

Thermal performance estimation for cryogenic storage tanks: Application to liquid hydrogen

Ailo Aasen^a, Sindre Stenen Blakseth^{a,b}, André Massing^b, Petter Neksa^a, Magnus Aa. Gjennestad^a

^a*SINTEF Energy Research, Trondheim, Norway*

^b*Department of Mathematical Sciences, Norwegian University of Science and Technology, Trondheim, Norway*

Abstract

The design of cryogenic liquid storage solutions requires accurate methods for estimating heat ingress, from the material level to the tank level. For insulation materials, thermal performance is usually measured using ambient conditions and liquid nitrogen at 77 K as boundary temperatures. A key question is how much heat ingress increases when storing liquid hydrogen (LH₂) at 20 K. We derive theoretical bounds on the increased heat ingress, and show that it remains below 26 %. Additionally, we demonstrate that heat ingress is much more sensitive to the warm boundary temperature than the cold boundary temperature. At the tank level, we compare two methods for assessing the steady-state thermal performance of cryogenic tanks: thermal network models and the heat equation solved with the finite element method. The latter offers high accuracy and adaptability for complex geometries, while thermal network models benefit from simplicity, speed and robustness. We apply both approaches to a self-supported LH₂ tank concept for maritime transport and analyze sensitivity to structural support thickness, warm boundary temperature, and choice of insulation material. The thermal network model can estimate heat ingress with $\sim 1\%$ error and the cold-spot temperature with error less than 1 K.

Keywords: Liquid hydrogen, Cryogenic storage tank, Heat ingress, Boil-off, Thermal network model, Finite element method

1. Introduction

A major hurdle for transitioning to renewable energy sources is that these sources do not necessarily provide energy exactly when or where it is needed. This challenge can be addressed through large-scale production, transport and storage of clean energy carriers, such as hydrogen (H₂) [1, 2, 3, 4, 5].

Hydrogen is an energy carrier that can serve as a clean and renewable fuel, but a hydrogen economy depends on effective storage and transport mechanisms. Since hydrogen gas at ambient conditions has a low density of 0.09 kg/m³, storing it in this state requires huge volumes. If local geological conditions permit, large-scale storage of gaseous hydrogen in salt caverns may be a cost-effective option [6, 3]. Another option is to increase density prior to storage. Strategies include chemically binding the hydrogen in liquid organic hydrogen carriers [7, 8], physisorption on metal-organic frameworks (MOFs) [9], compression and liquefaction [10, 11].

Liquefied hydrogen (LH₂) has a density at ambient pressure of 71 kg/m³, roughly three orders of magnitude higher than the gas phase (Tab. 1). LH₂ has exceptionally high purity, which after regasification enables direct use in high-purity applications such as fuel cells [1, 12]. Since the H₂ is not chemically bonded to heavy components (e.g. in NH₃) or adsorbed in other materials (e.g. MOFs), LH₂ has an unusually high gravimetric energy density and can be converted directly to pure H₂ gas without further processing. Since LH₂ can exist at ambient pressure, storage tanks can also be sized thinner than pressurized containers, reducing cost. An important drawback is hydrogen's extremely low normal boiling point of $-253\text{ }^\circ\text{C}$, and the large associated energy input required for the liquefaction process. With today's liquefaction technology, a third of the energy content of gaseous hydrogen is needed to liquefy it [13]. However, for large-scale optimized plants, it is predicted that this may be reduced to below 20 % [14, 15]. Moreover, some exergy invested into liquefaction can be reclaimed during regasification.

To make an LH₂ market economically feasible it must be scaled up by orders of magnitude, and a crucial technology gap is the development of

Email address: ailo.aasen@sintef.no (Ailo Aasen)

Table 1: Thermophysical properties of liquid hydrogen, liquid methane and liquid nitrogen at their respective normal boiling points ($p = 1$ atm). Here T is temperature, ρ is density, ΔH_{vap} is enthalpy of vaporization per liquid mass or volume, c_p is isobaric heat capacity, k is thermal conductivity, μ is viscosity, and γ is surface tension [16, 17, 18, 19].

	T K	ρ kg/m ³	ΔH_{vap} kJ/kg	ΔH_{vap} MJ/m ³	c_p kJ/kgK	k W/Km	μ μPa.s	γ mN/m
Hydrogen	20.4	70.8	449	31.8	9.77	0.104	13.5	1.91
Nitrogen	77.4	806	199	161	2.04	0.145	161	8.88
Methane	112	422	511	216	3.48	0.184	117	12.9

cost-effective large-scale storage tanks [20]. LH₂ must be stored in tanks with sophisticated insulation to limit boil-off, with tank design depending on the application [21]. The stationary tanks, and the mobile tanks on ships, aircraft, rockets, trains and trucks all feature different design problems related to loading/offloading, venting, optimal shape, sloshing and risks in general. Use of smaller stationary tanks is today routine, although tanks for large-scale LH₂ storage and transport similar to those used for liquefied natural gas (LNG), i.e. $\gtrsim 40\,000$ m³, have not yet been built. One challenge stems from the thermophysical peculiarities of LH₂, which are elucidated when compared to liquid methane and liquid nitrogen (Tab. 1). Its low boiling point temperature and low volumetric latent heat necessitate high thermal insulation performance [20].

Recently, there has been a surge of interest in the thermal modeling of liquid hydrogen tanks. Several studies focus on lumped-phase thermodynamic models for studying the pressurization rate and thermal stratification [22, 23, 24, 25, 26, 21, 27, 28]. Joseph et al. [22] observe that both effects increase with decreasing insulation thickness, but a crucial unknown is the rate of heat transport across the interface [23, 21, 27], which in practice is treated as a fudge factor tuned to experiments. Other studies focus more on the insulation [29, 30, 31, 32, 2, 33, 34, 35, 36], where the application of multi-layer insulation (MLI) and vapor-cooled shields are recurring topics. The general conclusion is that both MLI and vapor-cooled shields have a large potential to reduce boil-off, but their economic and technical feasibility for large-scale tanks is to date unresolved.

Yet other studies focus on the heat flow and temperatures in the insulation and tank, which are important issues to consider when analyzing thermal performance and thermal stresses. The work by Tapeinos et al. [37, 38, 39] combined experiments with finite element analysis of thermal and structural aspects for a novel LH₂ multi-sphere tank configuration. Johnson et al. [40] studied heat

transfer around localized hot and cold spots. Such spots may lead to increased thermal stresses while also affecting LH₂ flow patterns and heat transfer from the ambient. A recent work by Mantzaroudis and Theotokoglou [41] emphasizes that accounting for the temperature-dependence of thermophysical properties is crucial.

When optimizing an LH₂ tank design, models that are valid over a wide space of design parameters are needed. A notable recent work by Adler and Martins [21] presents an open-source tank model for liquid hydrogen storage which can be coupled with gradient-based optimization to find, e.g., the minimum weight for given storage restraints.

Use and transport of LH₂ in shipping is an emerging field receiving significant attention [42, 43, 20, 44, 45]. Already in 1998, Abe presented a conceptual design of a 200 000 m³ hydrogen tanker based on LNG technology. The use of LH₂ as maritime fuel holds the promise to eliminate harmful emissions from shipping, which corresponds to roughly 3% of global greenhouse gas emissions and more than 12% of SO_x and NO_x emissions [36]. Current bottlenecks include cost and lack of regulations, infrastructure, and qualification of materials [12, 36]. Ratnakar et al. [20] emphasized the possible advantages of LH₂ storage and transport due to the similarity with LNG technology and existing LH₂ technology in space programs. However, they noted that “for commercial widespread use and feasibility of hydrogen technology, it is of utmost importance to develop cost-effective and safe technologies for storage and transportation of LH₂ for use in stationary applications as well as offshore transportation.” They pointed to the need for reduced-order models that can easily analyze heat transport across a wide parameter space. Furthermore, they noted that while there is a significant amount of experimental data on the thermal performance of insulation materials in the literature, much of this is based on measurements with LN₂ and a cold boundary temperature (CBT) of 77 K. It is therefore some uncertainty as to how

these materials will perform in LH₂ applications with cold boundary temperatures down towards 20 K.

The present work aims to address some of these issues. First, in Sec. 2, we briefly reiterate some of the formalism of heat transport in insulation and solid materials and show that this immediately leads to some new insights when applied to LH₂ storage. In particular, we present a procedure to quantify the uncertainty in heat ingress that is a result of using models and measurements obtained with LN₂ and a CBT of 77 K. Next, we present a thermal network model, a type of reduced-order model, for cryogenic tanks that can account for cold spots through a correction. The numerical methods used are discussed in Sec. 3.

In Sec. 4, we test the presented procedure to quantify the uncertainty in heat ingress, apply it to several measurements and models available in the literature and discuss the results. We also argue that heat transport may be particularly sensitive to changes in the warm boundary temperature (WBT), and that cold spots induced by support structures acting as thermal bridges may therefore have an important impact on the total heat ingress.

In Sec. 5, we perform a case study where we apply the network model to a self-supported, non-pressurized tank intended for ship transport of LH₂. We compare the network model results to full solutions of the heat equation obtained with the finite element method (FEM). Finally, a sensitivity analysis on the selected case is performed and the impact of structural support size, ambient temperature and choice of insulation material is quantified. Furthermore, the uncertainty in total heat ingress and boil-off rate resulting from use of models and measurements based on experiments with LN₂ is presented and discussed.

2. Heat transfer modeling

In a piece of material placed between two heat baths at differing temperatures $T_c < T_w$, a heat flux \mathbf{q} will develop. For an insulation material, e.g. a porous bulk-fill material, this can be decomposed into contributions from gas conduction, solid conduction, gas convection and radiation,

$$\mathbf{q} = \mathbf{q}_{\text{cond}}^{\text{gas}} + \mathbf{q}_{\text{cond}}^{\text{sol}} + \mathbf{q}_{\text{conv}} + \mathbf{q}_{\text{rad}}. \quad (1)$$

Detailed modeling of each heat transfer mode can be complex and simpler models often offer sufficient accuracy. One common approach is to aggregate all modes into an equivalent conduction mode, having an apparent thermal conductivity

$k(T)$ defined through Fourier's law

$$\mathbf{q} = -k(T) \nabla T. \quad (2)$$

For a porous material the thermal conductivity also depends on the pressure p of the interstitial gas, i.e. $k(T, p)$. Unlike the temperature, however, the pressure p will generally be constant throughout the material. We can therefore write $k(T)$, with the understanding that this function is valid for a particular gas pressure. For a solid material, Eq. (2) can of course be used directly with k describing the thermal conductivity of the material.

In steady-state, local energy balance is described by $\nabla \cdot \mathbf{q} = 0$. Inserting Fourier's law (2) the energy balance equation becomes the steady-state heat equation,

$$\nabla \cdot (-k(T) \nabla T) = 0. \quad (3)$$

For Eq. (3) to have a unique solution, boundary conditions must be specified. For example, one may specify the boundary temperature (Dirichlet condition) or a temperature-independent heat flux (Neumann condition). Another option is a Robin condition, where the heat flux q normal to the boundary is determined by some convective heat transfer coefficient h and ambient temperature T_{amb} , so that

$$q = -k(T) \nabla T \cdot \mathbf{n} = h(T - T_{\text{amb}}). \quad (4)$$

Here, \mathbf{n} is the outward unit normal vector of the boundary.

2.1. Material properties

The apparent thermal conductivity of both insulation materials and structural materials can vary significantly between typical ambient temperatures and typical LH₂ storage temperatures [46], and we next consider models for this temperature dependence.

Hofmann [35] presented the following largely empirical model

$$k(T) = a + bT^c, \quad (5)$$

where a , b and c are parameters that need to be fitted to experimental results, and which implicitly are functions of the gas pressure. Hofmann fitted parameters for seven insulations: nitrogen gas at atmospheric pressure, evacuated perlite, evacuated microglass spheres, evacuated fibreglass, an evacuated multilayer insulation system, and a hypothetical insulation of ideally arranged reflectors in perfect vacuum.

NIST [47] has collected data on thermal conductivities of a range of structural and insulation

materials and give empirical models on the form

$$\log_{10}(k(T)) = \sum_{i=0}^N c_i (\log_{10}(T))^i, \quad (6)$$

where c_i are fitted parameters.

Ratnakar et al. [29] reviewed thermal conductivity modeling in cryogenic insulation materials, and introduced a first-principles-based functional form

$$k(T, p) = AT^m + BT^3 + \frac{CT^E}{1 + DT/p}. \quad (7)$$

Here m , A , B , C , D and E are non-negative parameters, which are independent of temperature and pressure. The first two terms account for solid conduction and radiation, respectively. The third term accounts for pressure-dependent gas conduction. In writing the conductivity as a sum of conductivities from different heat transfer modes, one implicitly assumes that the thermal resistances act in parallel with negligible coupling effects between the heat transfer modes.

The third term in Eq. (7) is the key innovation over Hofmann's correlation, as it incorporates the pressure-dependence explicitly. The functional form is inspired by kinetic gas theory, and corresponds to a gas conductivity $k^{\text{gas}}(T, p) = k_c(T)/(1 + \text{Kn})$, where $k_c(T) = CT^E$ is the pressure-independent continuum limit conductivity and $\text{Kn} = DT/p$ is the Knudsen number. Kn is the gas mean free path divided by the length scale of voids in the material. It is usually close to zero at atmospheric pressure, so that $k^{\text{gas}}(T, 1 \text{ atm}) \approx k_c(T)$. Since $k_c(T)$ is usually known, e.g. for helium, hydrogen and components of air, the temperature dependence E is taken as known. The prefactor C cannot be similarly deduced since it depends on the porosity of the material, with more voids implying more gas conduction heat transfer and thus a larger C .

2.2. Heat flow in one-dimensional geometries

One is often interested in steady-state heat flow through simple, effectively one-dimensional geometries between boundary temperatures T_c and T_w , e.g. normally through a planar slab or radially in a cylindrical or spherical geometry. Fourier's law (2) can then be integrated directly, yielding the well-known factorization of the heat flow Q as [46]

$$Q = S K(T_c, T_w), \quad (8)$$

where the thermal conductivity integral,

$$K = \int_{T_c}^{T_w} k(T) dT, \quad (9)$$

depends only on boundary temperatures and material properties, and the shape factor

$$S = \left(\int_{x_c}^{x_h} \frac{1}{A(x)} dx \right)^{-1}, \quad (10)$$

depends only on the geometry. Calculation of S requires an integral involving the area $A(x)$ between the positions x_c and x_h of the cold and warm boundaries. The quantity K , on the other hand, is a *geometry-independent* quantity that can be used to compare the thermal performance of materials. It follows from Eq. (8) that the SI value of K equals the heat flux (in W/m^2) through a 1 m thick slab.

The thermal conductivity integral can also be expressed by the *effective thermal conductivity*,

$$k_{\text{eff}}(T_c, T_w) = \frac{K(T_c, T_w)}{T_w - T_c}, \quad (11)$$

i.e. the average thermal conductivity over a temperature interval. For consistency one also defines $k_{\text{eff}}(T, T) = k(T)$. The quantities $k_{\text{eff}}(T_c, T_w)$ and $K(T_c, T_w)$ are equivalent in the sense that they both enable calculating the heat flow through a slab of material with boundary temperatures T_c and T_w . Using the effective thermal conductivity, one may rewrite Eq. (8) as

$$Q = \Delta T / R \quad (12)$$

where $\Delta T = T_w - T_c$ and the thermal resistance is

$$R = 1 / (S k_{\text{eff}}). \quad (13)$$

We stress that the heat flow factorization in Eq. (8) is derived assuming the validity of Fourier's law (2). That Fourier's law is valid even for a composite material having several modes of heat transfer leads to a significant simplification of heat flow calculations since local heat flow then depends only on local temperature and temperature gradients. In addition to simplifying thermal performance analysis, Eq. (8) also leads to some important insights for deep cryogenic applications, as we discuss next. To our knowledge these points have not previously been made in heat transfer textbooks [46, 48, 49] or in the research literature.

2.3. Concavity Hypothesis – Extrapolating measured thermal performance to LH_2 temperatures

Thermal performance measurements for cryogenic insulation materials are often made using experimental setups with CBT provided by liquid nitrogen (LN_2) at its normal boiling point of 77 K [20]. Using LN_2 for this purpose is convenient and repeating measurements with e.g. LH_2 is

more challenging and costly. Consequently, there is limited material property data available for thermal modeling of systems at or close to the boiling point temperature of LH₂ (20 K). This section offers a partial remedy. We shall consider what can still be inferred, with reasonable confidence, in spite of missing data for heat transfer with low CBTs. This will be done by giving upper and lower bounds for the heat ingress obtained when the CBT is reduced below temperatures for which one has reliable information.

We consider three temperatures $T_c < T_m < T_w$. Here, T_w now represents a typical ambient temperature (e.g. 293 K), T_c represents some low temperature (e.g. 20 K), and T_m some intermediate temperature (e.g. 77 K). We may assume that there is an underlying function describing the apparent thermal conductivity of the insulation material, for which we have some partial information. In the first case we only know the integral $K(T_m, T_w)$, obtained from measuring the heat flow through the material at a fixed CBT T_m (e.g. using an LN₂ cryostat). Another case is that we also know the underlying function $k(T)$, but only for temperatures down to T_m . We consider both cases here and consider what can still be inferred about the thermal performance in spite of missing information for temperatures below T_m .

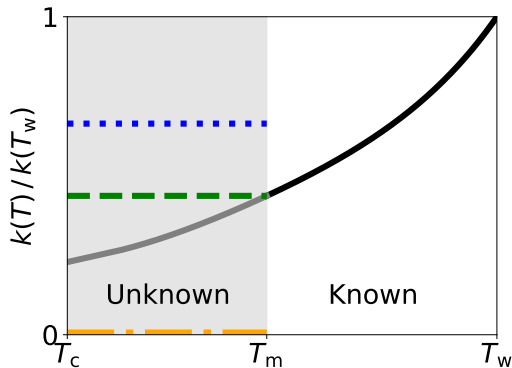


Figure 1: Illustration of normalized thermal conductivity $k(T)$ (black curve) and methods of extrapolating to low temperatures (colored curves). In the region between T_m and T_w (marked “known”), we know either the underlying function $k(T)$ or its integral $K(T_m, T_w)$. In the region between T_c and T_m (marked “unknown”), both are unknown. The blue dotted curve is the average value over the known region, the green dashed curve is the constant $k(T_m)$, and the orange dash-dotted curve is zero.

From Eq. (8), the heat ingress is determined by $K(T_c, T_w)$. It follows from Eqs. (9)–(11) that

$$K(T_c, T_w) = K(T_m, T_w) + k_{\text{eff}}(T_c, T_m)(T_m - T_c). \quad (14)$$

Herein, $K(T_m, T_w)$ now represents the thermal conductivity integral measured in cryostat experiments or the integral of the model $k(T)$ over its range of validity. To make further progress one must estimate $k_{\text{eff}}(T_c, T_m)$. We shall do this by supplying upper and lower bounds.

A lower bound follows from the fact that $k(T)$ is positive, and thus

$$k_{\text{eff}}(T_c, T_m) \geq 0. \quad (15)$$

This lower bound is illustrated as the dash-dotted orange line in Fig. 1 in relation to a hypothetical underlying function $k(T)$. In terms of the thermal conductivity integral this is equivalent to

$$K(T_c, T_w) \geq K_{\text{min}} = K(T_m, T_w). \quad (16)$$

The lower bound expresses that lowering the CBT will increase heat ingress.

To estimate an upper bound, we assume that the unknown underlying thermal conductivity $k(T)$ is a monotonically increasing function of temperature. This implies that $k_{\text{eff}}(T_c, T_m) \leq k_{\text{eff}}(T_m, T_1)$ whenever $T_m \leq T_1$, and hence any choice of T_1 will yield an upper bound. Choosing $T_1 = T_w$ yields

$$k_{\text{eff}}(T_c, T_m) \leq k_{\text{eff}}(T_m, T_w). \quad (17)$$

This upper bound is illustrated as the dotted blue line in Fig. 1. By inserting this bound into Eq. (14), we thus obtain

$$K(T_c, T_w) \leq K_{\text{max}}^{\text{int}}, \quad (18)$$

$$K_{\text{max}}^{\text{int}} = K(T_m, T_w) \frac{T_w - T_c}{T_w - T_m}.$$

We emphasize that $K_{\text{max}}^{\text{int}}$ may be obtained by a single heat flow measurement between T_m and T_w and may therefore be used when cryostat measurements of heat flow between these two temperatures are available. The superscript *int* alludes to it being proportional to the integral $K(T_m, T_w) = \int_{T_m}^{T_w} k(T) dT$.

If one has measured $k_{\text{eff}}(T_m, T_1)$ for decreasingly warm boundary temperatures T_1 , one obtains increasingly tight upper bounds. In the event that a model for $k(T)$ is known and valid down to a temperature T_m , one obtains the tightest bound when $T_1 = T_m$, namely

$$k_{\text{eff}}(T_c, T_m) \leq k_{\text{eff}}(T_m, T_m) = k(T_m). \quad (19)$$

This upper bound is illustrated as the dashed green line in Fig. 1. The corresponding upper bound on the thermal conductivity integral is given by

$$K(T_c, T_m) \leq K_{\text{max}}^{\text{diff}}, \quad (20)$$

$$K_{\text{max}}^{\text{diff}} = K(T_m, T_w) + k(T_m)(T_m - T_c).$$

The superscript *diff* indicates that it depends on differential information, as $k(T_m) = -(\partial K(T_m, T_c)/\partial T_m)_{T_c}$.

We now have that $K_{\min} \leq K \leq K_{\max}^{\text{diff}} \leq K_{\max}^{\text{int}}$. By multiplying with the shape factor S , we get for the heat ingress $Q = SK$ that

$$Q_{\min} \leq Q \leq Q_{\max}^{\text{diff}} \leq Q_{\max}^{\text{int}}, \quad \text{where} \quad (21)$$

$$Q_{\min} = Q(T_m, T_w), \quad (22)$$

$$Q_{\max}^{\text{diff}} = Q(T_m, T_w) - \left(\frac{\partial Q(T_m, T_w)}{\partial T_m} \right)_{T_w} (T_m - T_c), \quad (23)$$

$$Q_{\max}^{\text{int}} = Q(T_m, T_w) \frac{T_w - T_c}{T_w - T_m}. \quad (24)$$

An equivalent statement is that *heat flow is a decreasing, concave function of the cold boundary temperature*. We therefore refer to (21) as the Concavity Hypothesis. As it makes no reference to the apparent thermal conductivity k , it can also be applied to materials where it is unclear how to define k (e.g. MLI).

2.4. Network model

One way to estimate the heat ingress in more complex geometries, such as tanks, is to use a thermal network model. This is a well-established approach [24, 50] that makes some simplifying assumptions about the geometry and the available paths for heat flow. Here, we employ a version that accounts fully for the temperature dependence of the thermal conductivity.

The thermal network is made up of nodes, each with an index i and a temperature T_i . The nodes are connected by thermal resistances R_{ij} such that the heat flow Q_{ij} from node i to node j is

$$Q_{ij} = (T_i - T_j)/R_{ij}. \quad (25)$$

If nodes i and j are separated by a solid material, R_{ij} is given by Eq. (13). For a convective heat flow across a surface area A , heat flux is given by Eq. (4) and the corresponding thermal resistance is

$$R_{\text{conv}} = 1/(hA). \quad (26)$$

The energy balance for node i yields

$$\sum_j Q_{ij}(T_i, T_j) = 0, \quad (27)$$

where the sum is over all nodes j connected to i . Eq. (27) represents a set of non-linear equations that can be solved for the unknown node temperatures.

2.4.1. Cold spot estimation

In addition to calculating heat ingress, a thermal model should be able to describe cold spots in the structure. A cold spot may form, e.g., where a metallic support structure intersects with an outer part of the tank. Low cold-spot temperatures may result in ice formation, or even condensation of air, and cold spots can be associated with large temperature gradients and correspondingly high thermal stresses. Furthermore, an accurate prediction of cold spots will improve the accuracy of heat flow calculations for the thermal network model.

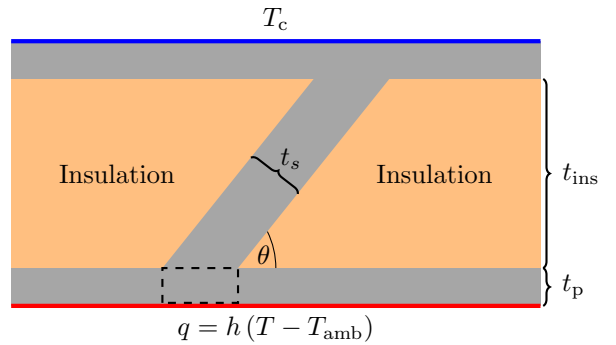


Figure 2: Schematic of the two-dimensional geometry considered in the cold spot estimation. Two parallel steel plates are connected by a supporting structure of thickness t_s , slanted at an angle θ . The remainder is filled with insulation. A Dirichlet boundary condition is applied to the cold surface (blue line), and a convective boundary coefficient to the ambient is applied at the warm surface (red line). A cold spot will develop in the dashed region where the support meets the warm plate.

A representative case that captures a source of cold spots is the effectively two-dimensional geometry shown in Fig. 2: Two plates, one warm and one cold, have an insulation material between them and are connected by a support structure of thickness t_s . The two plates are separated by a distance t_{ins} and the warm plate has thickness t_p . To avoid considering boundary effects, we assume the plates extend to infinity in the horizontal directions. The inside of the cold plate is assumed to be at a constant temperature T_c , while the outside of the warm plate exchanges heat with the ambient temperature so that the heat flux across it is given by (4).

To a first approximation, the temperature in the warm plate is uniform in the direction normal to the plate, and only a function $T(\xi)$ of the distance ξ along the plate, away from the cold spot. Letting $T_\infty = \lim_{\xi \rightarrow \infty} T(\xi)$ and $\Delta T(\xi) = T(\xi) - T_\infty$, one

can derive the approximation

$$\Delta T(\xi) = \Delta T(0) \exp(-|\xi|/\Xi), \quad (28)$$

$$\Xi = \sqrt{k_p(T_\infty)t_p/(h + k_{\text{ins}}(T_\infty)/t_{\text{ins}})}, \quad (29)$$

where k_p and k_{ins} are the thermal conductivities of the warm plate and the insulation, respectively and length scale Ξ describes how big the cold spot will be. The heat flow through the warm plate into the cold spot is given by

$$Q_{\text{cs}} = -\frac{\Delta T(0)}{R_{\text{cs}}}, \quad (30)$$

where

$$R_{\text{cs}} = \frac{\Xi}{2Lt_pk_p(T_\infty)}, \quad (31)$$

and L is the length of the connection between the support and the warm plate, i.e. the thickness of the two-dimensional geometry depicted in Fig. 2.

A cold-spot correction is added to the network model by introducing a resistance given by Eq. (31). We give a concrete example of its application in Sec. 5, and we shall see that the correction indeed gives more accurate heat flow estimates. In addition, Eq. (28) can be used for estimating temperature profiles near a cold spot. Both equations, however, require the faraway temperature T_∞ , which can be calculated in different ways. When a resistance R_{cs} is included in the network model, T_∞ is obtained as part of the solution. This results, however, in a slight underestimation of T_∞ . To estimate the temperature profile $T(\xi)$ using Eq. (28), we therefore first solve a network model without support structure to get T_∞ .

Local corrections such as the one presented here to account for the cold spot are a standard tool in thermal engineering that can be derived for various geometries, e.g., to describe heat dissipation in fins [48]. A detailed derivation and further validation of accuracy can be found in the Supplementary Information (SI).

3. Numerical methods

In this section, we briefly describe the numerical methods used to solve the thermal network model and the heat equation.

3.1. Network model

The network model consists of a non-linear system of equations (27) for the unknown node temperatures. These were solved iteratively by successively solving linearized approximations to Eq. (27), with constant resistances. In each iteration, thermal resistances were updated using the

current node temperatures and then the linear system was solved using DGEV from the LAPACK library [51], called through the NumPy [52]. Iteration continued until the node temperatures converged.

Once the network model is solved, temperature profiles $T(x)$ along individual resistances in the network may be obtained. This was here accomplished by splitting the resistance under considerations into N resistances in series. Then, starting at the cold side temperature, Eq. (12) was solved for ΔT for each resistance in succession, thus obtaining the temperature at the $N - 1$ intermediate nodes.

3.2. Heat equation

This section describes how we solve the steady-state heat equation (3) numerically using the finite element method. Let Ω be the domain on which we want to solve the equation (i.e., the cryogenic tank, including insulation and support structure), and let Γ_D and Γ_R denote the parts of domain boundary where we impose Dirichlet and Robin boundary conditions, respectively. On the remainder of the boundary, we impose homogeneous Neumann conditions (i.e., zero heat flux). For a given simplicial mesh $\mathcal{T}_h = \{\tau\}$ of Ω and prescribed temperature T_D on Γ_D , we define the trial function space $V_{h,T_D} = \{f \in C(\Omega) \mid f|_\tau \in \mathbb{P}^3(\tau) \forall \tau \in \mathcal{T}_h \text{ and } f|_{\Gamma_D} = T_D\}$ and its corresponding test function space $V_{h,0}$, where $\mathbb{P}^3(\tau)$ is the space of cubic polynomials defined on the mesh element τ . Then, the *discrete weak formulation* of Eq. (3), supplemented with the Robin boundary condition of Eq. (4), reads: Find $T_h \in V_{h,T_D}$ such that

$$\int_{\Omega} k(T_h) \nabla T_h \cdot \nabla v_h \, dx + \int_{\Gamma_R} h T_h v_h \, ds = \int_{\Gamma_R} h T_{\text{amb}} v_h \, ds \quad (32)$$

for all test functions $v_h \in V_{h,0}$.¹ We handle the non-linearity in Eq. (32) resulting from the temperature dependence of k through linearization and Newton iterations. Mesh creation, linearization, assembly of a linear system of equations representing Eq. (32), and solution of the assembled system of equations, are all handled within the open-source finite element software suite Netgen/NGSolve [53, 54], which we access through its Python interface. Since the tanks considered herein are rotationally symmetric, we express Eq. (32) using cylindrical coordinates and

¹Since the containment system is made from multiple materials, k is discontinuous across material interfaces.

use a two-dimensional mesh (visualized in the Supplementary Information) for increased computational efficiency. The mesh consists of 147 989 elements over which we define third-order basis functions (cf. the definitions of V_{h,T_d} and $V_{h,0}$ above). Curved domain surfaces are approximated to the third order using NGSolve’s in-built functionality for curved element facets.

Given the computed temperature field T_h , we estimate the heat ingress by

$$Q_h = \int_{\Gamma_{\text{in}}} \mathcal{P}^1 \{-k(T_h) \nabla T_h \cdot \mathbf{n}\} ds, \quad (33)$$

where $\mathcal{P}^1 \{\cdot\}$ denotes projection into the space of continuous, elementwise linear functions, Γ_{in} is the tank’s inner surface, and \mathbf{n} is its surface normal vector pointing into the contained LH₂. The integral in Eq. (33) was evaluated numerically using NGSolve.

4. Implications of material properties on heat ingress

In this section, we explore selected aspects of the relationship between material properties and heat ingress. We evaluate the validity of the Concavity Hypothesis for a selection of materials relevant to LH₂ applications, and discuss its implications for uncertainty in insulation performance predictions. We also show that the material-specific dependence of apparent thermal conductivity on temperature has important implications for overall thermal performance and sensitivity to boundary conditions.

4.1. Validity of the Concavity Hypothesis

The thermal conductivities $k(T)$ of a number of insulation materials are plotted in Fig. 3. It is readily observed that the thermal conductivities are all monotonically increasing. This implies that the Concavity Hypothesis is valid for these materials. For the materials where $k(T)$ is known reliably down to 20 K, we have verified this observation numerically by calculating the thermal conductivity integral K as well as the lower and upper bounds from Sec. 2.3. We used 77 K as the intermediate temperature T_m when computing the bounds. The results are shown in Tab. 2, where a selection of structural materials, such as aluminum 5083 (Al5083) and stainless steel 316 (SS316), are also included. For all the examples listed, $K_{\text{min}} \leq K \leq K_{\text{max}}^{\text{diff}} \leq K_{\text{max}}^{\text{int}}$, meaning that the Concavity Hypothesis is valid. It is also evident that $K_{\text{max}}^{\text{diff}}$, in addition to being an upper bound, is in fact an excellent approximation to K .

The Concavity Hypothesis is valid for many materials relevant to LH₂ applications, as demonstrated above. However, caveats are warranted for three notable cases.

First, for some solid materials, thermal conductivity can have a non-monotonic temperature dependence. A prominent example is pure copper, which experiences a strong increase in thermal conductivity in the 20 K-range [55]. A similar effect can also be observed in other pure metals, such as aluminum [56]. On the other hand, metallic alloys, such as Al5083 and SS316 have numerous grain boundaries that limit electronic heat transfer and are expected to have monotonically increasing thermal conductivities [46]. Hence, the hypothesis holds for these materials, as previously noted.

The second caveat pertains to porous insulation materials at intermediate vacuum levels. The insulation materials in Tab. 2 are evaluated in either the high-pressure or the low-pressure limit, which are the scenarios typically considered in applications. As we have seen, the Concavity Hypothesis works well in these scenarios. Moreover, the hypothesis’ key assumption that $k(T)$ be monotonic is consistent with all published measurements on insulation materials known to the authors. However, as exemplified by the Ratnakar correlation [29], thermal conductivity can in principle become slightly non-monotonic in the intermediate pressure range where gas conduction is strongly pressure-dependent (the Knudsen regime). An example of this is shown in the SI.

Finally, natural convection is a potential concern in non-evacuated insulation materials. As temperature decreases from LN₂ to LH₂, the Rayleigh number increases and may exceed the critical Rayleigh number for the establishment of convection cells [57]. Since the Rayleigh number is proportional to the characteristic length scale, porous insulation materials with small void spaces are less susceptible to this effect. Cracks and defects in the insulation, however, can promote convection.

4.2. Application of the Concavity Hypothesis

For the insulation materials considered in Tab. 2, both the thermal conductivity integrals K (20 K, 293 K) and their corresponding bounds are visualized in Fig. 4. The figure also includes bounds, derived using the Concavity Hypothesis, for insulation materials whose exact K (20 K, 293 K) is not known.

Fig. 4 offers a robust clarification of the relative performance of different insulation materials. The performance differences can be gleaned even from the red error bars alone, obtained by a single measurement between a CBT of 77 K and a WBT of

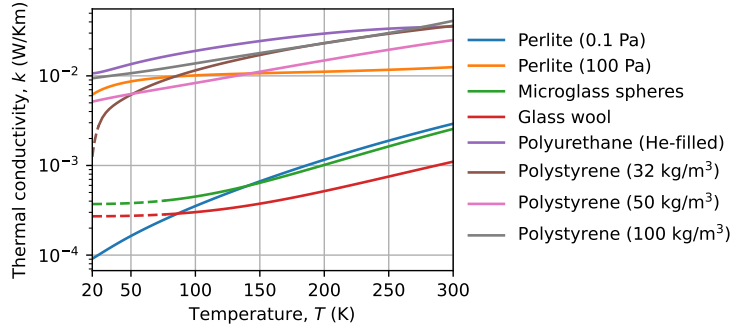


Figure 3: Thermal conductivities of insulation materials as a function of temperature, where the dashed portions represent extrapolations of the thermal conductivity correlations below their range of validity. Perlite correlations are from Ref. [29], Microglass spheres and Glass wool correlations from Ref. [35], and the remaining correlations from Ref. [47].

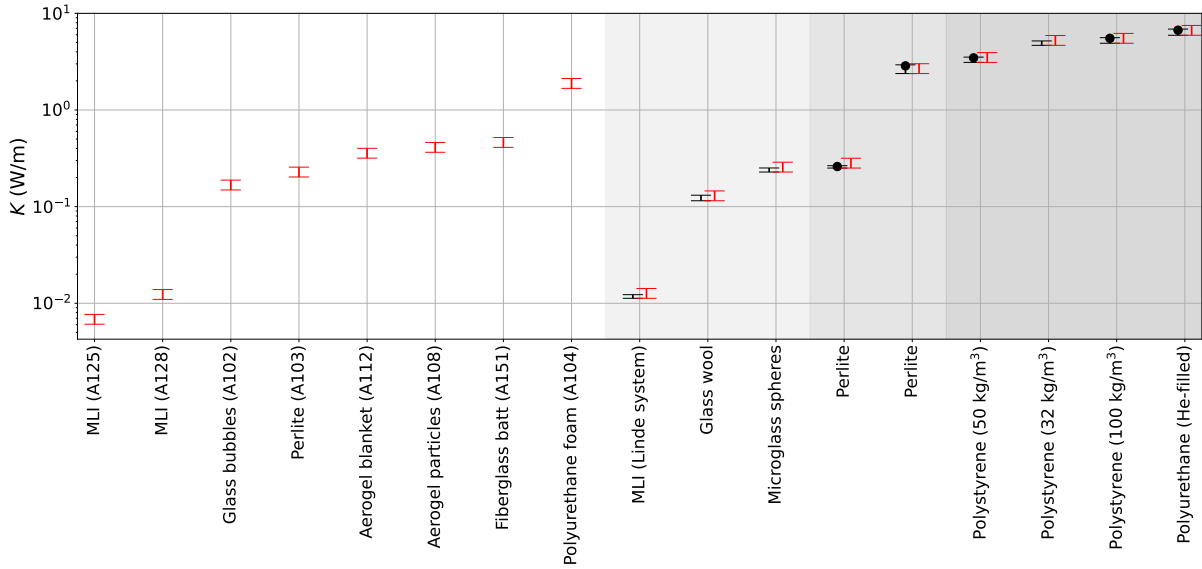


Figure 4: Thermal conductivity integral for insulation materials between 20 K and 293 K. The black dots correspond to the actual value of K in the case it is known from measurements. The black interval corresponds to the bounds one can derive if the thermal conductivity is known at 77 K, whereas the red intervals correspond to the bounds one can derive from a single heat ingress measurement between 77 K and 293 K. The different background shades correspond to different references, which are, from left to right: [58], [35], [29], [47]. The warm temperature 293 K was chosen since this was the temperature used in the measurements by Fesmire [58]. The identifiers (A125 etc.) correspond to the indexing scheme by Fesmire [58].

293 K. This indicates that uncertainty due to the CBT of measurements is unlikely to significantly affect the overall performance hierarchy. Additionally, as previously noted, the difference between K (the black dots) and K_{\max}^{diff} (the upper black error bar) is small. This excellent agreement is quantified in Tab. 2, with relative errors below 5%, and indicates that K_{\max}^{diff} is a practically useful estimate of K .

Generally, when only a single measurement of heat flow through a material is available, the Concavity Hypothesis can still provide useful insights. According to Eq. (24), the global upper bound only depends on the boundary temperatures. In particular, for $T_c = 20$ K, $T_c = 77$ K, $T_w = 293$ K, we obtain that the heat ingress increases by no more than 26 % when lowering the CBT from LN₂ to LH₂ temperatures. The average of the upper and lower bounds in Tab. 2, which corresponds to a 13 % increase, can be used as a rule-of-thumb for the increase in heat ingress when translating from LN₂ to LH₂ applications when only a single heat ingress measurement has been performed.

Another application of the Concavity Hypothesis is in the design of experiments. These are often done using LN₂ at its boiling point as the CBT. It is, however, of interest to know the heat ingress for lower temperatures as well. Although the 13 % rule of thumb can be used, Q_{\max}^{diff} is a better estimate that is both accurate and also conservative (i.e. an overestimate). To calculate Q_{\max}^{diff} , it follows from Eq. (23) that one must estimate $\partial Q(T_m, T_{\text{amb}})/\partial T_m$. If an experimental setup is used with LN₂ at atmospheric pressure, i.e. $T_m = 77$ K, one can obtain a slightly higher CBT by increasing the pressure of the nitrogen in the tank. For LN₂, the saturation temperature increases with roughly 6 K/bar, and therefore another measurement with 2 bar internal tank pressure may suffice to estimate the derivative.

4.3. Sensitivity of heat ingress to boundary temperatures

One aspect that follows immediately from Eqs. (8) and (9) is the sensitivity of $Q(T_c, T_w)$ to the boundary temperatures T_c and T_w . Differentiating Eq. (8) and dividing by Q , we get that the relative change in heat ingress is independent of the geometry, and given by

$$\frac{1}{Q} \left(\frac{\partial Q}{\partial T_w} \right)_{T_c} = \frac{k(T_w)}{K(T_c, T_w)}, \quad (34)$$

$$\frac{1}{Q} \left(\frac{\partial Q}{\partial T_c} \right)_{T_w} = \frac{-k(T_c)}{K(T_c, T_w)}. \quad (35)$$

Since the thermal conductivity of many materials is a strongly increasing function of temperature,

this implies that the WBT has a much larger impact on the heat ingress than does the CBT.

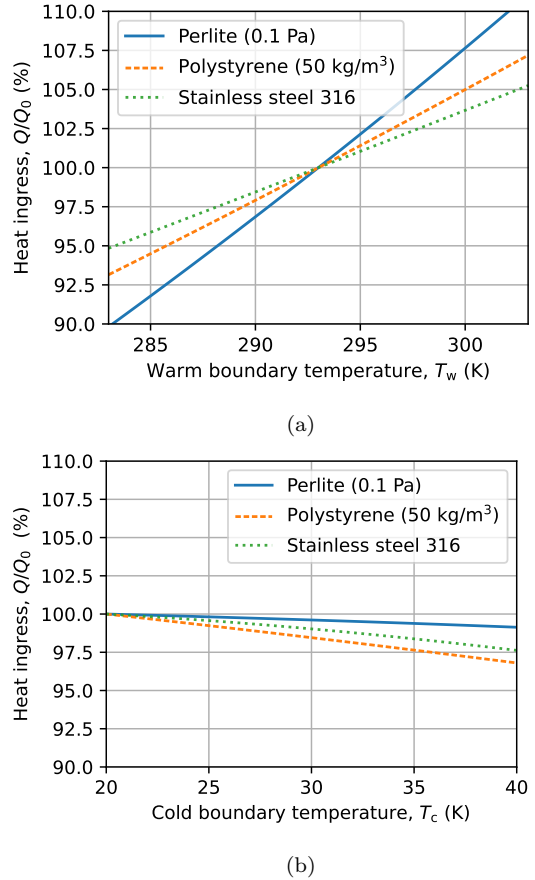


Figure 5: Response in heat ingress $Q(T_w, T_c)$ through three materials when (a) varying T_w , keeping $T_c = 20$ K, and (b) varying T_c , keeping $T_w = 293$ K. In both cases, the heat ingress Q has been normalized by $Q_0 = Q(T_c = 20 \text{ K}, T_w = 293 \text{ K})$.

Fig. 5 shows how heat ingress varies with respect to changes in the WBT and CBT for rectangular slabs made from two example insulation materials (evacuated perlite and polystyrene) and a structural material (SS316). As expected from Eqs. (34) and (35), the heat ingress is much less sensitive to the CBT than to the WBT. We find the same to be true also for the other materials listed in Tab. 2. For perlite the relative increase in heat ingress is on the order of 1% per Kelvin increase in WBT, whereas the sensitivity for the CBT is an order of magnitude lower.

The observation above has at least three implications of great practical importance. First, it means that ambient conditions should be carefully considered when designing LH₂ tanks and related infrastructure. Secondly, it implies that comparatively low thermal conductivity at higher temperatures is an attractive feature in insulation materials, due to its large impact on K . Thirdly,

Table 2: The thermal conductivity integral $K = K(20\text{ K}, 293\text{ K})$ for LH₂ and ambient boundary temperatures, as well as the bounds calculated from information in the interval [77 K, 293 K]. Here $K_{\min} = K(77\text{ K}, 293\text{ K})$ and the quantities K_{\max}^{diff} and K_{\max}^{int} correspond to the theoretical upper bounds Eq. (20) and Eq. (18), respectively.

Material	K_{\min} (W/m)	K (W/m)	K_{\max}^{diff} (W/m)	K_{\max}^{int} (W/m)	Ref.
Perlite (0.1 Pa)	0.251	0.260	0.265	0.317	[29]
Perlite (100 Pa)	2.38	2.86	2.93	3.01	[29]
Perlite (1 bar)	5.90	6.59	6.82	7.46	[29]
Polyurethane (He-filled)	5.93	6.69	6.87	7.49	[47]
Polystyrene (100 kg/m ³)	4.90	5.51	5.60	6.20	[47]
Polystyrene (50 kg/m ³)	3.10	3.46	3.52	3.92	[47]
Aluminum 5083	20000	22200	23100	25300	[47]
Stainless steel 316	2600	2910	3050	3280	[47]
Fiberglass (normal direction)	92.5	106	108	117	[47]
Teflon	56.4	67.9	69.6	71.3	[47]

thermal performance can only be estimated accurately if the warm boundary surface temperature is suitably represented in the thermal model used. For thermal network models, this provides a clear theoretical motivation for including the cold spot correction presented in Sec. 2.4.1. The practical benefit of this correction is investigated in Sec. 5.1.

5. Case study of self-supported spherical tank

In this section we study the heat ingress, boil-off rate and temperature distribution in a particular tank geometry. For this purpose, we employ the network model, both with and without the cold-spot correction, and the heat equation solved with the FEM. A detailed discussion of the results and a comparison of the modeling approaches is done in Sec. 5.1. In Sec. 5.2 we consider the effect of changing the dimensions of the support structure, the effect of changes in the ambient temperature and the effect of choosing different insulation materials.

The considered tank is intended for ship transport of LH₂ and is a 40 000 m³ spherical double-jacketed and vacuum insulated tank supported with a cylindrical skirt. It is similar in structure to the tank design developed by Moss Maritime, described in the patent application in Skogan et al. [59]. The specific dimensions of tank components chosen here are considered to be structurally viable, but not necessarily optimal, for an LH₂ tank.

The tank consists of four basic parts: (1) A spherical inner tank made from stainless steel 316 (SS316) with internal radius of 21.2 m and a thickness of 5 cm, (2) a spherical outer tank made from carbon steel with internal radius 22.25 m and a thickness of 5 cm, (3) a cylindrical support skirt

with a thickness of $t_{\text{supp}} = 6.5\text{ cm}$ made from SS316 that connects the equatorial part of the inner tank to the outer tank and (4) an annular space in between the inner and outer tank that contains insulation material. In addition, the skirt is connected to the inner tank by an equatorial ring and to the outer tank by a cylindrical mounting ring. The latter mounting ring extends slightly outside the outer tank to form an interface towards the ship's inner hull. The geometry is rotationally symmetric and is illustrated in Fig. 6. The mesh used when solving the heat equation with the FEM is illustrated in the SI.

Stainless steel is considered a relevant example material for the inner tank and the support skirt. It is a class of alloys viewed as compatible with hydrogen [60], and it has been used successfully by NASA in their LH₂ storage tanks at Kennedy Space Center [61]. Furthermore, it is a deliberate choice to consider a support skirt made of the same material as the inner tank. This eliminates the need to have joints between different materials in the coldest regions of the tank, which may be problematic due to different thermal expansion properties [62, p. 129].

In calculations, the thermal conductivity of SS316 is modeled by Eq. (6) with parameters from [47], while the thermal conductivity of carbon steel is set to 51.9 W/(m K). Furthermore, the temperature of the inner wall of the inner tank is kept constant at $T_c = 20\text{ K}$. At the outer wall of the outer tank, a convective boundary condition is used, with heat transfer coefficient $h = 2.5\text{ W}/(\text{m}^2\text{ K})$ and $T_{\text{amb}} = 293\text{ K}$. The interface to the ship hull is assumed adiabatic.

From the heat ingress Q into a cryogenic storage tank one may estimate the boil-off rate (BOR) by dividing by the latent enthalpy of vaporization. This implicitly assumes no superheating of the gas

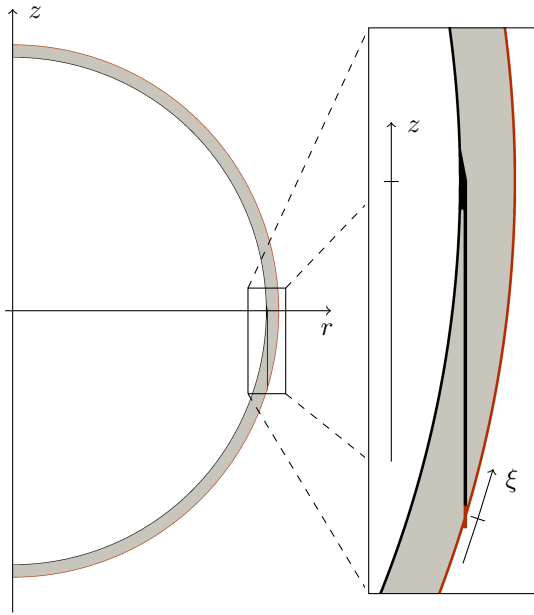


Figure 6: Illustration of the spherical LH_2 tank. The inner tank, the equatorial ring and support skirt are made of stainless steel 316 (black), the outer tank and mounting ring of carbon steel (red) and the annulus is filled with insulation material (gray). The inset shows a close-up of the support skirt. The z -coordinate indicates vertical position, with $z = 0$ at the equatorial line. The coordinate ξ denotes the distance along the outer tank wall from the intersection between the skirt and the outer tank.

that is let out of the tank to keep pressure constant at 1 atm. The BOR is commonly measured as the mass of liquid evaporated per time relative to the mass of liquid in a full tank,

$$\text{BOR} = \frac{Q}{\rho V \Delta H}, \quad (36)$$

where ρ is the liquid density, V is the tank volume, and ΔH is the specific latent heat. The typical unit is percent per day (%/d).

5.1. Heat ingress and cold spot calculation

In this section, we calculate the heat ingress and temperature distribution for the tank geometry described in the previous section, with perlite insulation at a pressure of 10^{-2} Pa. We employ the network model, both with and without the cold-spot correction, and the heat equation solved with the FEM. The same tank geometry is represented in all three models, the same boundary conditions are applied and the same material thermal conductivity models are used. The thermal conductivity of perlite is modeled by Eq. (7) with parameters from [29].

While the network model represents a simplified version of the geometry, the heat equation resolves additional details. In particular, the equatorial ring that connects the inner tank with the skirt and the mounting ring are not included in the network model, and the height $L_{\text{supp}} = 5.672$ m of the skirt in the network model is the corresponds to the distance between the equatorial ring and the mounting ring.

The networks used are illustrated in Fig. 7. The resistances R_{inner} , R_{ins} , R_{supp} and R_{outer} were calculated using Eq. (13) and represent, respectively, the inner tank, the insulation, the support skirt and the outer tank. The resistance R_{conv} represents convective resistance to the ambient (see Eq. (26)) and R_{cs} models heat flow into the cold spot (see Eq. (31)).

The resulting heat ingress and cold-spot temperature from the three different models are given in Tab. 3. It can be seen that the uncorrected network model over-predicts the heat ingress by 2.8%, w.r.t. the results from the heat equation. By accounting for the cold-spot, however, the over-prediction is reduced by one order of magnitude, to 0.3%.

The BOR is estimated to be approximately 0.04%/d. This is in the lower range of what is assumed in many high-level value chain studies in the literature, which ranges from 0.03%/d to 1.35%/d [63]. It is, however, in line with what can be expected when the benefit of scale, i.e. small surface-to-volume ratio, is combined with

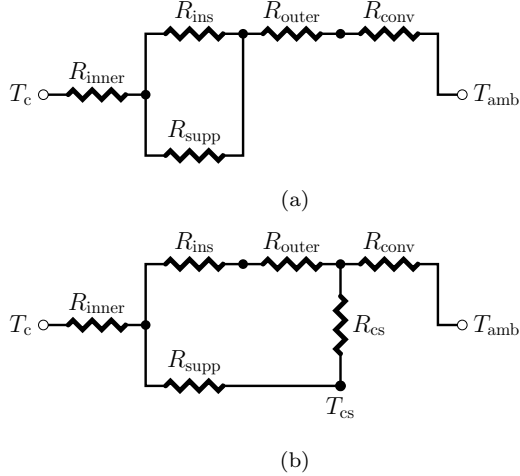


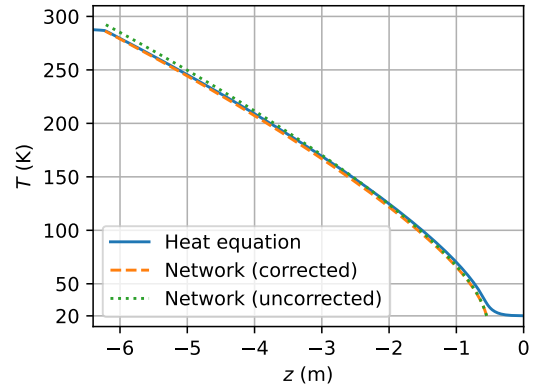
Figure 7: Representations of the spherical LH₂ tank in (a) the uncorrected network model and (b) the corrected network model. In both networks, each node represents a temperature. The white nodes have specified temperatures while the model needs to be solved to get the temperatures in the black nodes. In (b), the thermal resistance R_{cs} corresponds to heat flow into the cold spot.

the assumption that the same vacuum conditions are attainable for the large tank under consideration here as in smaller tanks currently in operation [63, 20].

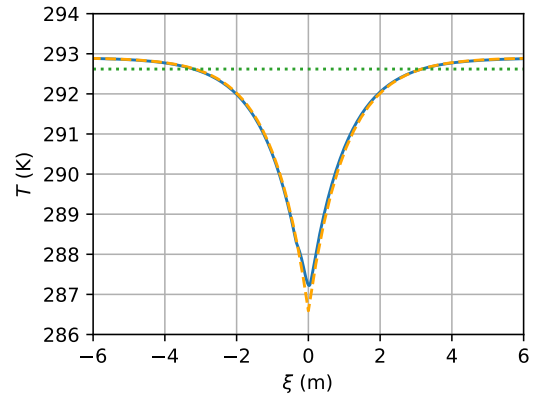
The uncorrected network model does not incorporate the effect of the cold spot and therefore, as can be seen in Tab. 3, does not predict any reduction in temperature at the cold spot. The corrected network model, on the other hand, accurately reproduces the cold-spot temperature from the heat equation. From Tab. 3, the deviation in cold-spot temperature between the heat equation and the corrected network model is only 0.6 K.

Three temperature profiles in the support skirt, along the vertical direction, are shown in Fig. 8a. These profiles were computed with, respectively, the heat equation, the corrected network model and the uncorrected network model. All three curves have a steeper gradient at cold temperatures due to the lower thermal conductivity of SS316 in this region. Furthermore, all three models roughly agree on the temperature variation along the skirt. However, the two network models do not accurately reproduce the heat equation profile near the innermost edge of the skirt where the skirt is connected to the support ring. This is a result of the simplified treatment of the structural geometry by the network model in this region. Near the outermost end of the skirt, the corrected model agrees very well with the heat equation results, while the uncorrected model does not.

Three temperature profiles in the outer tank, as a function of distance from the point where the outer tank and the skirt intersects, are shown in Fig. 8b. These profiles were again computed with the heat equation, the corrected network model and the uncorrected network model, respectively. The corrected network model captures not only the cold spot temperature, but also the variation in outer tank temperature and the temperature at the cold spot very well.



(a)



(b)

Figure 8: Temperature distribution in (a) the support skirt as a function of vertical position z and (b) the outer tank as a function of distance ξ from the cold spot. In both plots, results from the heat equation (FEM) are shown in solid blue, results from the corrected network model in dashed orange and results from the uncorrected network model in dotted green.

From the results presented in this section, we conclude that the corrected network model accurately reproduces the results from full solutions of the heat equation for the heat ingress, the cold spot temperature and the variation in temperature along the outer tank wall.

Table 3: Results for total heat ingress Q , heat ingress through support Q_{supp} , cold spot temperature T_{cs} and BOR for the network model (corrected and uncorrected) and heat equation (FEM).

	Q (kW)	Q_{supp} (kW)	T_{cs} (K)	BOR (%/d)
Network (uncorr.)	5.953	4.444	292.6	0.0405
Network (corr.)	5.809	4.298	286.6	0.0395
Heat eqn.	5.789	-	287.2	0.0394

5.2. Sensitivity analysis

In this section we use the three methods for heat ingress calculation to study the effect of three important parameters: (1) the skirt thickness, (2) the ambient air temperature and (3) choice of insulation material. We thus assess the ability of the two variants of the network model to predict how the heat ingress depends on these parameters. In the case of insulation material, we also illustrate the uncertainty in heat ingress resulting from using insulation thermal conductivity measurements and models that are not valid for CBTs down to 20 K.

Effect of skirt dimensions. For the case discussed in the preceding section, approximately 70 % of the heat ingress was transmitted through the support skirt. It is therefore of interest to consider how the heat ingress varies with skirt dimensions.

The variation of heat ingress and BOR with skirt thickness is shown in Fig. 9 for calculations performed with the heat equation and the corrected and uncorrected network models. It is seen that the total heat ingress increases approximately 0.7 kW per cm of skirt thickness. This increase is accurately captured by the corrected network model, while the uncorrected network model over-predicts the heat ingress.

In varying the skirt thickness t_{supp} , the inner radius of the skirt is kept fixed and the outer radius is changed. This leads to a slight reduction in the skirt height L_{supp} as the thickness is increased. In Fig. 9 the result of scaling the heat ingress in the support with the skirt thickness t_{supp} , and the inverse of the skirt height L_{supp} , is shown as a dash-dotted black line. This line agrees reasonably well with both the corrected network model and the heat equation results. This agreement shows that most of the change in heat ingress can be attributed directly to the resulting change in shape factor S in the skirt, while the resulting changes in boundary temperatures and the thermal conductivity integral K are less important.

Effect of ambient temperatures. As we showed in Sec. 4.3, the heat ingress through both insulation

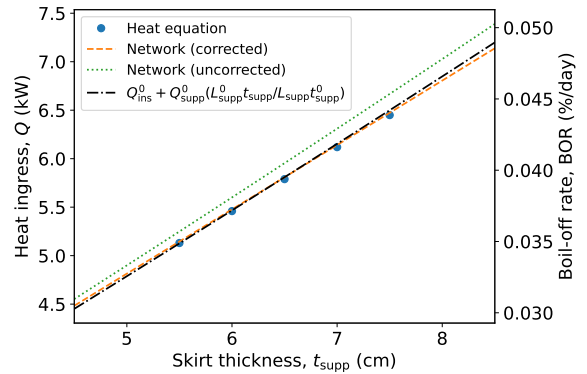


Figure 9: Variation in heat ingress and BOR with thickness t_{supp} of the support skirt in the LH₂ tank case. The increase in skirt thickness is also associated with a slight reduction of skirt height L_{supp} . Results are obtained with the heat equation (blue dots), the network model with cold-spot correction (dashed orange) and the network model without cold-spot correction (dotted green). In addition, the total heat ingress and BOR obtained when scaling the heat flow Q_{supp}^0 through a support of thickness $t_{\text{supp}}^0 = 6.5$ cm and length L_{supp}^0 with the factor $L_{\text{supp}}^0 t_{\text{supp}} / L_{\text{supp}} t_{\text{supp}}^0$ is shown (dash-dotted black). The insulation heat flow Q_{ins}^0 is calculated with support dimensions t_{supp}^0 and L_{supp}^0 .

and structural materials in LH₂ tanks may be sensitive to ambient temperatures. For a ship traversing the globe, the ambient temperatures will vary along its route and it is therefore important to consider the effect of ambient temperatures on heat ingress and BOR.

The variation of heat ingress and boil-off rates with ambient temperature are shown in Fig. 10. The heat ingress and BOR changes considerably, by approximately 30 %, when the ambient temperature increases from 0 °C to 40 °C. As was the case when varying skirt dimensions, the corrected network model accurately reproduces the results from the heat equation, while the uncorrected network model over-predicts heat ingress and boil-off rates.

The changes in ambient temperature do not affect any of the shape factors in the network model, only the thermal conductivity integrals of the different resistances. According to Eq. (34), this variation can be approximated by the thermal conductivity evaluated at the changing boundary temperature multiplied with the perturbation in that temperature. Using this approximation, for both the insulation and the support yields the black dash-dotted line in Fig. 10. This accurately reproduces the smaller perturbations in ambient temperature. It is less accurate for larger perturbations with a visible difference for changes larger than approximately 10 K.

The changes in ambient conditions in this section is limited to the effect of convective heat transfer between the outside of the tank and the ambient temperatures. In addition, there would be varying influx of solar radiation due to changing sky conditions. We do not consider such effects here, but only mention that they are expected to further exacerbate the fluctuations in heat ingress and BOR.

Effect of different insulation materials. An important factor in the design of a cryogenic storage tank is, of course, choice of insulation material. In this section, we use data and models from different literature sources [29, 58, 35, 47] for the thermal properties of various insulation material and calculate the effect on heat ingress and BOR in the LH₂ tank case. Calculations were performed with the corrected network model. For the cases involving MLL, we have assumed that the thickness of insulation is the same that is given in the original sources. The insulation materials from [29, 58, 35] are here considered for pressures below 1.3×10^{-2} Pa.

The variation of heat ingress and boil-off rates from different choices of insulation material is shown in Fig. 11. The various insulation materials correspond to a large range of boil-off rates, from

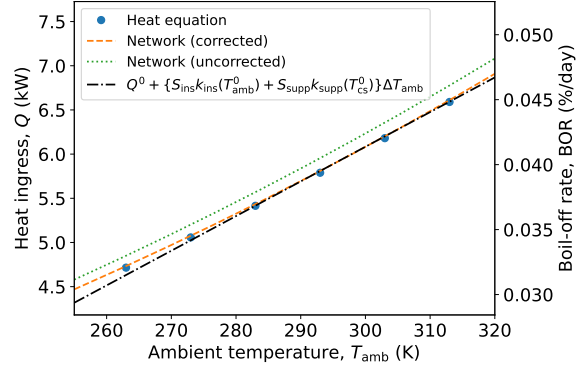


Figure 10: Variation of heat ingress and BOR with ambient temperature T_{amb} in the LH₂ tank case. Results are obtained with the heat equation (blue dots), the network model with cold-spot correction (dashed orange) and the network model without cold-spot correction (dotted green). In addition, the heat ingress obtained when applying Eq. (34) to the insulation and the support is shown (dash-dotted black). Herein, Q^0 is the total heat ingress and T_{cs}^0 the cold spot temperature at $T_{\text{amb}} = 293$ K. Furthermore, S_{ins} is the shape factor of the insulation, S_{supp} is shape factor of the support, k_{ins} is the thermal conductivity of the insulation, k_{supp} is the thermal conductivity of the support and $\Delta T_{\text{amb}} = T_{\text{amb}} - T_{\text{amb}}^0$.

the lowest 0.036 %/d (glass bubbles) to 0.3 %/d (Helium-filled polyurethane foam).

NASA has made extensive studies of cryogenic insulation performance, much of which is summarized in [58]. The measurements presented there were all performed with 77 K as the CBT. To use these measurements in the present case, with a cold CBT of 20 K, leads to some uncertainty in the heat ingress and BOR. This uncertainty was evaluated using Eq. (17), and is illustrated as orange error bars in Fig. 11. In contrast, Hofmann [35] present thermal conductivity models that are stated to be valid down to CBTs of 77 K. Their corresponding uncertainty when reducing the CBT to 20 K were calculated using Eq. (20) and are illustrated with red error bars in Fig. 11. From this figure, it is evident that knowing k at 77 K, and thus being able to use $K_{\text{max}}^{\text{diff}}$ (see Eq. (20)) as upper bound rather than $K_{\text{max}}^{\text{int}}$ (see Eq. (17)), significantly reduces the uncertainty. The models from [47] and [29] are valid down to 20 K, or close to it, and thus have no or negligible uncertainty.

NASA has published several papers comparing the thermal performance of perlite powder and glass bubbles, see e.g. [58, 64], and have found that glass bubbles perform significantly better. Sass et al. found a reduction in LH₂ BOR of 34 % in 1 m³ demonstration tanks when perlite was replaced

with glass bubbles [65] and found a reduction of 44% in a field-scale tank [64]. In the present case, the reduction in heat ingress through the insulation is smaller, approximately 27%. Furthermore, this case also has a significant heat ingress through the support skirt which is largely unaffected by the choice of insulation material. The result is that the reduction in total heat ingress and BOR (see Fig. 11) is only 7%.

For most insulation materials in Fig. 11 there is little or no overlap of the error bars. Thus, the uncertainty introduced by using thermal performance measurements with 77 K as the CBT in the present case is of limited importance for the qualitative comparison of material performance in the tank considered. However, the error bars may still represent a significant uncertainty in the values of the various heat ingress and boil-off rates. For the materials from [58] they are in the range of 4–16%, while for those from [35] it is only 2%. For those from [47], uncertainties are negligible.

One way to reduce the uncertainty is to obtain accurate thermal properties also in the temperature region between 77 K and 20 K for insulation materials where they are not available. However, for the results from [58], uncertainty can also be reduced as described in section Sec. 4.2, without the need to do experiments with a CBT of 20 K.

The rightmost point in Fig. 11 corresponds to Helium-filled polyurethane foam. This is an unevacuated insulation material with a fill gas that does not condense or freeze at LH₂ temperatures. Evacuated insulation materials exhibit excellent thermal performance, but requires a structure that can hold the vacuum and withstand buckling induced by the ambient pressure. Using non-evacuated insulation materials has many advantages, as pointed out in [57]. One advantage is that the outer tank would then face a smaller pressure difference between the insulation and the ambient, and thus be less prone to buckling. The outer tank may then be made from a thinner layer of material. This can particularly be important for large tanks since they can become heavy if they rely on an evacuated double-wall structure [20]. Other advantages could include improved safety, reduced cost, and no time needed for establishing a vacuum by pumping. As we see from Fig. 11, however, this comes at a cost of higher heat ingress and BOR. Compared to the base case of evacuated perlite, the BOR is more than seven times higher. Still, the rate of 0.3%/d may be within the range that could be utilized for ship propulsion [57].

6. Summary and conclusions

Measurements of heat transfer through cryogenic insulation materials are often made with liquid nitrogen (LN₂) at 77 K as the cold boundary temperature (CBT). This work addressed the uncertainty in thermal performance if these materials are applied to liquid hydrogen (LH₂) storage, where the CBT is often around 20 K. Specifically, we introduced the Concavity Hypothesis, which states that the heat ingress is a concave, decreasing function of the CBT. The Concavity Hypothesis relies on the observation that thermal conductivity tends to be monotonically increasing with temperature. This assumption was tested and found to be valid for a number of available thermal conductivity correlations that are valid down to 20 K, and we have argued that it is expected to be generally valid for evacuated insulation materials.

Assuming a warm boundary temperature of ~ 293 K, changing the CBT from 77 K to 20 K resulted in an increase in the heat ingress from the ambient below 20% in materials where reliable thermal conductivity models are available (cf. Tab. 2). Using the Concavity Hypothesis, we derived an upper bound, Q_{\max}^{int} , of 26% increase, and suggested using half of this (13% increase) as a rule-of-thumb. A tighter upper bound, Q_{\max}^{diff} , is available if one knows the material's thermal conductivity at 77 K. We found that this bound may serve as an accurate *estimate* of the heat ingress, with relative errors below 5%. This clearly motivates the measurement of thermal conductivity at 77 K, and we outlined a possible experimental procedure to do so.

We found that the heat transfer through a material is often much more sensitive to perturbations in the temperature on the warm side than on the cold side. This means that, when selecting LH₂ insulation materials, low thermal conductivity at high temperatures is decisive. Using perlite as an example, we found that for small variations in the ambient temperature, the heat ingress increased with as much as 1% per Kelvin. This insight motivated studying the effect on heat transfer through cold spots on the outside of tanks introduced e.g. by structural support elements.

We next employed a thermal network model to analyze a cryogenic storage tank designed for the large-scale maritime transport of LH₂. The network model was enhanced with a correction to account for the impact of external cold spots on the total heat ingress and to assess the temperature distribution near such cold spots. The model's predictions were validated against finite element method (FEM) solutions of the steady-state heat equation, showing excellent agreement with errors

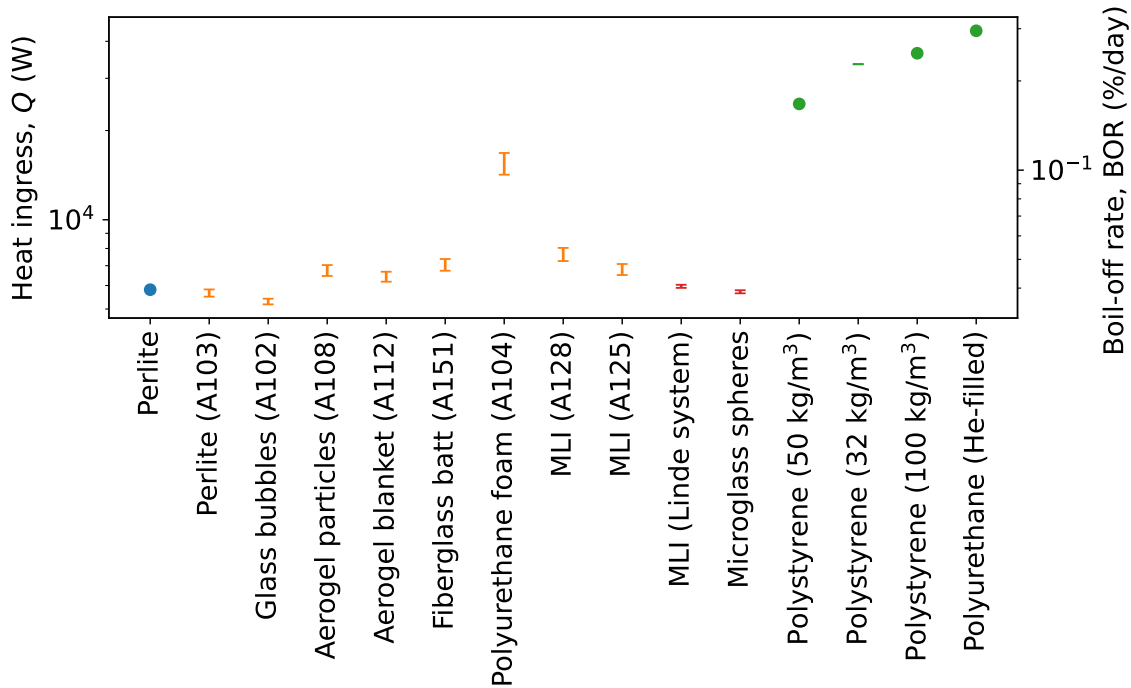


Figure 11: Heat ingress and BOR resulting from different choices of insulation materials in the LH₂ tank case. Insulation thermal conductivity data/models are from [29] (blue), [58] (orange), [35] (red) and [47] (green). The error bars represent the uncertainty in the total heat ingress resulting from using insulation thermal conductivity measurements that have been performed with 77 K rather than 20 K as CBT. The WBT is 293 K. The identifiers (A103 etc.) correspond to the indexing scheme by Fesmire [58].

in total heat ingress and cold spot temperatures within 0.3 % and 0.6 K, respectively.

Both the network model and the FEM solutions of the heat equation were used to quantify the effects of support thickness and ambient temperatures on heat ingress and boil-off. The network model, with the cold spot correction, was shown to predict these variations well. A notable finding was a potential increase in boil-off rates up to 30 % under plausible ambient temperature changes.

Finally, we used the network model to assess the effect of using different insulation materials for the considered tank. While evacuated insulation materials achieve the lowest boil-off, non-evacuated insulation systems nevertheless appear promising if the boil-off gas could be utilized for e.g. ship propulsion.

Acknowledgments

This publication is based on results from the research project *LH₂ Pioneer – Ultra-insulated seaborne containment system for global LH₂ ship transport*, performed under the ENERGIX program of the Research Council of Norway. The authors acknowledge the following parties for financial support: Gassco, Equinor, Air Liquide, HD Korea Shipbuilding & Offshore Engineering,

Moss Maritime and the Research Council of Norway (320233).

CRedit authorship contribution statement

Ailo Aasen: Conceptualization; Formal analysis; Investigation; Methodology; Software; Supervision; Validation; Visualization; Writing - original draft; and Writing - review & editing. **Sindre Stenen Blakseth:** Conceptualization; Formal analysis; Investigation; Methodology; Software; Validation; Visualization; Writing - original draft; and Writing - review & editing. **André Massing:** Funding acquisition; Methodology; Supervision; Writing - review & editing. **Petter Nekså:** Funding acquisition; Supervision; Writing - review & editing. **Magnus Aa. Gjennestad:** Conceptualization; Formal analysis; Investigation; Methodology; Project administration; Software; Supervision; Validation; Visualization; Writing - original draft; and Writing - review & editing.

References

- [1] D. Stolten, B. Emonts, Hydrogen Science and Engineering: Materials, Processes, Systems and Technology, Wiley, 2016. doi:10.1002/9783527674268. URL <http://dx.doi.org/10.1002/9783527674268>

- [2] L. Yin, H. Yang, Y. Ju, Review on the key technologies and future development of insulation structure for liquid hydrogen storage tanks, *International Journal of Hydrogen Energy* 57 (2024) 1302–1315. doi:10.1016/j.ijhydene.2024.01.093. URL <http://dx.doi.org/10.1016/j.ijhydene.2024.01.093>
- [3] N. Ma, W. Zhao, W. Wang, X. Li, H. Zhou, Large scale of green hydrogen storage: Opportunities and challenges, *International Journal of Hydrogen Energy* 50 (2024) 379–396. doi:10.1016/j.ijhydene.2023.09.021. URL <http://dx.doi.org/10.1016/j.ijhydene.2023.09.021>
- [4] P. Muthukumar, A. Kumar, M. Afzal, S. Bhogilla, P. Sharma, A. Parida, S. Jana, E. A. Kumar, R. K. Pai, I. Jain, Review on large-scale hydrogen storage systems for better sustainability, *International Journal of Hydrogen Energy* 48 (85) (2023) 33223–33259. doi:10.1016/j.ijhydene.2023.04.304. URL <http://dx.doi.org/10.1016/j.ijhydene.2023.04.304>
- [5] G. K. Karayel, N. Javani, I. Dincer, A comprehensive assessment of energy storage options for green hydrogen, *Energy Conversion and Management* 291 (2023) 117311.
- [6] J. Andersson, S. Grönkvist, Large-scale storage of hydrogen, *International Journal of Hydrogen Energy* 44 (23) (2019) 11901–11919. doi:10.1016/j.ijhydene.2019.03.063.
- [7] P. Preuster, C. Papp, P. Wasserscheid, Liquid organic hydrogen carriers (LOHCs): Toward a hydrogen-free hydrogen economy, *Accounts of Chemical Research* 50 (1) (2017) 74–85. doi:10.1021/acs.accounts.6b00474.
- [8] J. Zheng, H. Zhou, C.-G. Wang, E. Ye, J. W. Xu, X. J. Loh, Z. Li, Current research progress and perspectives on liquid hydrogen rich molecules in sustainable hydrogen storage, *Energy Storage Materials* 35 (2021) 695–722.
- [9] J. Park, J. Ha, R. Muhammad, H. K. Lee, R. Balderas-Xicohtencatl, Y. Cheng, A. J. Ramirez-Cuesta, B. Streppel, M. Hirscher, H. R. Moon, H. Oh, 20 K H₂ physisorption on metal-organic frameworks with enhanced dormancy compared to liquid hydrogen storage, *ACS Applied Energy Materials* 6 (18) (2022). doi:10.1021/acsaem.2c01907.
- [10] S. Krasae-in, J. H. Stang, P. Neksa, Development of large-scale hydrogen liquefaction processes from 1898 to 2009, *International Journal of Hydrogen Energy* 35 (10) (2010) 4524–4533. doi:10.1016/j.ijhydene.2010.02.109.
- [11] S. Z. Al Ghafri, S. Munro, U. Cardella, T. Funke, W. Notardonato, J. P. M. Trusler, J. Leachman, R. Span, S. Kamiya, G. Pearce, A. Swanger, E. D. Rodriguez, P. Bajada, F. Jiao, K. Peng, A. Siahvashi, M. L. Johns, E. F. May, Hydrogen liquefaction: a review of the fundamental physics, engineering practice and future opportunities, *Energy & Environmental Science* 15 (7) (2022) 2690–2731. doi:10.1039/d2ee00099g.
- [12] F. Ustolin, A. Campari, R. Taccani, An extensive review of liquid hydrogen in transportation with focus on the maritime sector, *Journal of Marine Science and Engineering* 10 (9) (2022) 1222. doi:10.3390/jmse10091222.
- [13] D. O. Berstad, J. H. Stang, P. Neksa, Comparison criteria for large-scale hydrogen liquefaction processes, *International Journal of Hydrogen Energy* 34 (3) (2009) 1560–1568. doi:10.1016/j.ijhydene.2008.11.058.
- [14] U. Cardella, L. Decker, J. Sundberg, H. Klein, Process optimization for large-scale hydrogen liquefaction, *International Journal of Hydrogen Energy* 42 (17) (2017) 12339–12354. doi:10.1016/j.ijhydene.2017.03.167.
- [15] Ø. Wilhelmsen, D. Berstad, A. Aasen, P. Neksa, G. Skaugen, Reducing the exergy destruction in the cryogenic heat exchangers of hydrogen liquefaction processes, *International Journal of Hydrogen Energy* 43 (10) (2018) 5033–5047. doi:10.1016/j.ijhydene.2018.01.094.
- [16] J. W. Leachman, R. T. Jacobsen, S. G. Penoncello, E. W. Lemmon, Fundamental equations of state for parahydrogen, normal hydrogen, and orthohydrogen, *Journal of Physical and Chemical Reference Data* 38 (3) (2009) 721–748. doi:10.1063/1.3160306.
- [17] R. Span, E. W. Lemmon, R. T. Jacobsen, W. Wagner, A. Yokozeki, A reference equation of state for the thermodynamic properties of nitrogen for temperatures from 63.151 to 1000 k and pressures to 2200 mpa, *Journal of Physical and Chemical Reference Data* 29 (6) (2000) 1361–1433. doi:10.1063/1.1349047. URL <http://dx.doi.org/10.1063/1.1349047>
- [18] U. Setzmann, W. Wagner, A new equation of state and tables of thermodynamic properties for methane covering the range from the melting line to 625 k at pressures up to 1000 mpa, *Journal of Physical and Chemical Reference Data* 20 (6) (1991) 1061–1155. doi:10.1063/1.555898. URL <http://dx.doi.org/10.1063/1.555898>
- [19] I. H. Bell, J. Wronski, S. Quoilin, V. Lemort, Pure and pseudo-pure fluid thermophysical property evaluation and the open-source thermophysical property library CoolProp, *Industrial & Engineering Chemistry Research* 53 (6) (2014) 2498–2508. doi:10.1021/ie4033999.
- [20] R. R. Ratnakar, N. Gupta, K. Zhang, C. van Doorne, J. Fesmire, B. Dindoruk, V. Balakotaiah, Hydrogen supply chain and challenges in large-scale LH₂ storage and transportation, *International Journal of Hydrogen Energy* (2021). doi:10.1016/j.ijhydene.2021.05.025.
- [21] E. J. Adler, J. R. A. Martins, Liquid hydrogen tank boil-off model for design and optimization, *Journal of Thermophysics and Heat Transfer* (November 2024).
- [22] J. Joseph, G. Agrawal, D. K. Agarwal, J. Pisharady, S. Sunil Kumar, Effect of insulation thickness on pressure evolution and thermal stratification in a cryogenic tank, *Applied Thermal Engineering* 111 (2017) 1629–1639. doi:10.1016/j.applthermaleng.2016.07.015.
- [23] S. Z. S. Al Ghafri, A. Swanger, V. Jusko, A. Siahvashi, F. Perez, M. L. Johns, E. F. May, Modelling of liquid hydrogen boil-off, *Energies* 15 (3) (2022) 1149. doi:10.3390/en15031149.
- [24] A. Majumdar, T. Steadman, J. Maroney, J. Sass, J. Fesmire, Numerical modeling of propellant boil-off in a cryogenic storage tank, in: *AIP Conference Proceedings*, Vol. 985, American Institute of Physics, 2008, pp. 1507–1514. doi:10.1063/1.2908513.
- [25] S. Barsi, M. Kassemi, Numerical and experimental comparisons of the self-pressurization behavior of an LH₂ tank in normal gravity, *Cryogenics* 48 (2008) 122–129. doi:10.1016/j.cryogenics.2008.01.003.
- [26] S. Barsi, M. Kassemi, Investigation of tank pressurization and pressure control—Part II: numerical modeling, *Journal of Thermal Science and Engineering Applications* 5 (4) (2013) 041006. doi:10.1115/1.4023892.
- [27] K. I. Matveev, J. W. Leachman, The effect of liquid hydrogen tank size on self-pressurization and constant-pressure venting, *Hydrogen* 4 (3) (2023) 444–455. doi:10.3390/hydrogen4030030. URL <http://dx.doi.org/10.3390/hydrogen4030030>

- [28] E. Mendez Ramos, Enabling conceptual design and analysis of cryogenic in-space vehicles through the development of an extensible boil-off model (2021).
- [29] R. R. Ratnakar, Z. Sun, V. Balakotaiah, Effective thermal conductivity of insulation materials for cryogenic LH₂ storage tanks: A review, *International Journal of Hydrogen Energy* 48 (21) (2023) 7770–7793. doi:10.1016/j.ijhydene.2022.11.130.
- [30] G. Babac, A. Sisman, T. Cimen, Two-dimensional thermal analysis of liquid hydrogen tank insulation, *International Journal of Hydrogen Energy* 34 (2009) 6357–6363. doi:10.1016/j.ijhydene.2009.05.052.
- [31] J. Zheng, L. Chen, J. Wang, X. Xi, H. Zhu, Y. Zhou, J. Wang, Thermodynamic analysis and comparison of four insulation schemes for liquid hydrogen storage tank, *Energy Conversion and Management* 186 (2019) 526–534. doi:10.1016/j.enconman.2019.02.073.
- [32] J. Zheng, L. Chen, C. Cui, Y. Zhou, J. Wang, Calculation and position optimization on vapor cooled shield for liquid hydrogen storage, in: *IOP Conference Series: Materials Science and Engineering*, Vol. 502, 2019, p. 012080. doi:10.1088/1757-899X/502/1/012080.
- [33] W. Jiang, P. Sun, P. Li, Z. Zuo, Y. Huang, Transient thermal behavior of multi-layer insulation coupled with vapor cooled shield used for liquid hydrogen storage tank, *Energy* 231 (2021) 120859. doi:10.1016/j.energy.2021.120859. URL <http://dx.doi.org/10.1016/j.energy.2021.120859>
- [34] Z. Liu, Y. Li, F. Xie, K. Zhou, Thermal performance of foam/mli for cryogenic liquid hydrogen tank during the ascent and on orbit period, *Applied Thermal Engineering* 98 (2016) 430–439.
- [35] A. Hofmann, The thermal conductivity of cryogenic insulation materials and its temperature dependence, *Cryogenics* 46 (2006) 815–824. doi:10.1016/j.cryogenics.2006.08.001.
- [36] Z. Wang, Y. Wang, S. Afshan, J. Hjalmarsson, A review of metallic tanks for h₂ storage with a view to application in future green shipping, *International Journal of Hydrogen Energy* (2020).
- [37] I. G. Tapeinos, S. Koussios, R. M. Groves, Design and analysis of a multi-cell subscale tank for liquid hydrogen storage, *International Journal of Hydrogen Energy* 41 (5) (2016) 3676–3688. doi:10.1016/j.ijhydene.2015.10.104.
- [38] I. G. Tapeinos, D. S. Zarouchas, O. K. Bergsma, S. Koussios, R. Benedictus, Evaluation of the mechanical performance of a composite multi-cell tank for cryogenic storage: Part I - Tank pressure window based on progressive failure analysis, *International Journal of Hydrogen Energy* 44 (7) (2019) 3917–3930. doi:10.1016/j.ijhydene.2018.12.118.
- [39] I. G. Tapeinos, A. Rajabzadeh, D. S. Zarouchas, M. Stief, R. M. Groves, S. Koussios, R. Benedictus, Evaluation of the mechanical performance of a composite multi-cell tank for cryogenic storage: Part II – Experimental assessment, *International Journal of Hydrogen Energy* 44 (7) (2019) 3931–3943. doi:10.1016/j.ijhydene.2018.12.063.
- [40] W. Johnson, R. Balasubramaniam, R. Grotenrath, Analysis of heat transfer from a local heat source at cryogenic temperatures, in: *IOP Conference Series: Materials Science and Engineering*, Vol. 1240, 2022, p. 012013. doi:10.1088/1757-899X/1240/1/012013.
- [41] V. K. Mantzaroudis, E. E. Theotokoglou, Computational analysis of liquid hydrogen storage tanks for aircraft applications, *Materials* 16 (6) (2023). doi:10.3390/ma16062245.
- [42] A. Abe, M. Nakamura, I. Sato, H. Uetani, T. Fujitani, Studies of the large-scale sea transportation of liquid hydrogen, *International Journal of Hydrogen Energy* 23 (1998) 115–121. doi:10.1016/s0360-3199(97)00032-3.
- [43] R. Scurlock, Problems of bulk storage and shipping of liquid hydrogen in volumes of 10,000 to 100,000 cubic meters at one bar pressure, in: *Cryogenics 2017. Proceedings of the 14th IIR International Conference*, International Institute of Refrigeration, 2017, pp. 140–144. doi:10.18462/iir.cryo.2017.0001.
- [44] A. N. Alkhaledi, S. Sampath, P. Pilidis, A hydrogen fuelled LH₂ tanker ship design, *Ships and Offshore Structures* 17 (7) (2022) 1555–1564. doi:10.1080/17445302.2021.1935626.
- [45] V. Cristea, Storage tank concepts for liquefied hydrogen, Master’s thesis, Norwegian University of Science and Technology (2020).
- [46] R. F. Barron, G. F. Nellis, *Cryogenic heat transfer*, CRC press, 2017.
- [47] NIST, *Cryogenic technology resources - Material properties* (2021). URL <https://trc.nist.gov/cryogenics/materials/materialproperties.htm>
- [48] F. P. Incropera, D. P. DeWitt, T. L. Bergman, A. S. Lavine, *Fundamentals of heat and mass transfer*, 6th Edition, Wiley, 2007.
- [49] J. H. Lienhard IV, J. H. Lienhard V, *A Heat Transfer Textbook*, 5th Edition, Phlogiston Press, 2019.
- [50] O. T. Ogunsola, L. Song, Application of a simplified thermal network model for real-time thermal load estimation, *Energy and buildings* 96 (2015) 309–318. doi:10.1016/j.enbuild.2015.03.044.
- [51] E. Anderson, Z. Bai, C. Bischof, S. Blackford, J. Demmel, J. Dongarra, J. Du Croz, A. Greenbaum, S. Hammarling, A. McKenney, D. Sorensen, *LAPACK Users’ Guide*, 3rd Edition, Society for Industrial and Applied Mathematics, Philadelphia, PA, 1999.
- [52] C. R. Harris, K. J. Millman, S. J. van der Walt, R. Gommers, P. Virtanen, D. Cournapeau, E. Wieser, J. Taylor, S. Berg, N. J. Smith, R. Kern, M. Picus, S. Hoyer, M. H. van Kerkwijk, M. Brett, A. Haldane, J. F. del Río, M. Wiebe, P. Peterson, P. Gérard-Marchant, K. Sheppard, T. Reddy, W. Weckesser, H. Abbasi, C. Gohlke, T. E. Oliphant, Array programming with NumPy, *Nature* 585 (7825) (2020) 357–362. doi:10.1038/s41586-020-2649-2. URL <https://doi.org/10.1038/s41586-020-2649-2>
- [53] J. Schöberl, NETGEN An advancing front 2D/3D-mesh generator based on abstract rules, *Computing and Visualization in Science* 1 (1997) 41–52. doi:10.1007/s007910050004.
- [54] J. Schöberl, C++ 11 implementation of finite elements in NGSolve, *Tech. Rep. 30/2014*, Institute for analysis and scientific computing – Vienna University of Technology (2014).
- [55] N. J. Simon, E. S. Drexler, R. P. Reed, Properties of copper and copper alloys at cryogenic temperatures. final report, *Tech. rep.* (2 1992). doi:10.2172/5340308.
- [56] A. L. Woodcraft, Recommended values for the thermal conductivity of aluminium of different purities in the cryogenic to room temperature range, and a comparison with copper, *Cryogenics* 45 (9) (2005) 626–636. doi:10.1016/j.cryogenics.2005.06.008.
- [57] R. R. Ratnakar, S. Sharma, M. Taghavi, V. Balakotaiah, A short discussion on insulation strategies and design considerations for large-scale storage and transportation of liquid hydrogen, *Energy Systems* (2023) 1–13doi:10.1007/s12667-023-00649-1.
- [58] J. E. Fesmire, Standardization in cryogenic insulation systems testing and performance data, *Physics Procedia* 67 (2015) 1089–1097. doi:10.1016/j.phpro.2015.06.205.

- [59] T. Skogan, J. Hveem, F. Fløtten, J. Anker, Liquified gas storage tank, patent application no. NO 20221390. Norwegian Industrial Property Office, 2022-12-22. URL <https://search.patentstyret.no/Patent/20221390>
- [60] C. San Marchi, B. P. Somerday, Technical reference for hydrogen compatibility of materials, Tech. rep., Sandia National Laboratories, SAND2012-7321 (2012).
- [61] A. G. Krenn, Diagnosis of a poorly performing liquid hydrogen bulk storage sphere, in: AIP conference proceedings, Vol. 1434, American Institute of Physics, 2012, pp. 376–383. doi:10.1063/1.4706942.
- [62] T. D. Bostock, R. G. Scurlock, *Low-Loss Storage and Handling of Cryogenic Liquids*, Springer, 2019.
- [63] D. Berstad, S. Gardarsdottir, S. Roussanaly, M. Voldund, Y. Ishimoto, P. Nekså, Liquid hydrogen as prospective energy carrier: A brief review and discussion of underlying assumptions applied in value chain analysis, *Renewable and Sustainable Energy Reviews* 154 (2022) 111772. doi:10.1016/j.rser.2021.111772.
- [64] J. Sass, W. S. Cyr, T. Barrett, R. Baumgartner, J. Lott, J. Fesmire, Glass bubbles insulation for liquid hydrogen storage tanks, in: AIP Conference Proceedings, Vol. 1218, American Institute of Physics, 2010, pp. 772–779. doi:10.1063/1.3422430.
- [65] J. Sass, J. Fesmire, Z. Nagy, S. Sojourner, D. Morris, S. Augustynowicz, Thermal performance comparison of glass microsphere and perlite insulation systems for liquid hydrogen storage tanks, in: AIP conference proceedings, Vol. 985, American Institute of Physics, 2008, pp. 1375–1382. doi:10.1063/1.2908497.